Cellulose (2021) 28:9441–9460
https://doi.org/10.1007/s10570-021-04129-6

ORIGINAL RESEARCH

Addition of $Al(OH)_3$ versus AlO(OH) nanoparticles on the optical, thermo-mechanical and heat/oxygen transmission properties of microfibrillated cellulose films

Tjaša Kolar · Branka Mušič · Romana Cerc Korošec · Vanja Kokol

Received: 17 March 2021 / Accepted: 2 August 2021 / Published online: 12 August 2021

Abstract Differently structured aluminum (tri/-mono) hydroxide ($Al(OH)_3$ /AlO(OH)) nanoparticles were prepared and used as thermal-management additives to microfibrillated cellulose (MFC), cast-dried in thin-layer films. Both particles increased the thermal stability of the MFC film, yielding 20–23% residue at 600 °C, and up to 57% lowered enthalpy (to 5.5–7.5 kJ/g) at 0.15 wt% of loading, while transforming to alumina (Al_2O_3). However, the film containing 40 nm large $Al(OH)_3$ particles decomposed in a one-step process, and released up to 20% more energy between 300 and 400 °C as compared to the films prepared from smaller (21 nm) and metastable AlO(OH), which decomposed gradually with an exothermic peak shifted to 480 °C. The latter resulted in a highly flexible, optically transparent (95%), and mechanically stronger (5.7 GPa) film with a much lower specific heat capacity (0.31–0.28 J/gK compared to 0.68–0.89 J/gK for MFC-$Al(OH)_3$ and 0.87–1.26 for MFC films), which rendered it as an effective heat-dissipating material to be used in flexible opto-electronics. Low oxygen permeability (2192.8 cm^3/m^2day) and a hydrophobic surface (> 60°) also rendered such a film useful in ecologically-benign and thermosensitive packaging.

Keywords Microfibrillated cellulose · Aluminum hydroxide nanoparticles · Transparent films · Mechanical properties · Thermal management · Oxygen and heat transmission

T. Kolar · V. Kokol (✉)
Faculty of Mechanical Engineering, University of Maribor, Smetanova ulica 17, 2000 Maribor, Slovenia
e-mail: vanja.kokol@um.si

B. Mušič
Nanotesla Institute Ljubljana, Stegne 29, 1000 Ljubljana, Slovenia

R. C. Korošec
Faculty of Chemistry and Chemical Technology, University of Ljubljana, Večna pot 113, 1000 Ljubljana, Slovenia

Introduction

Nano and micro-fibrillated cellulose are becoming important low cost, lightweight and renewable nanomaterials, being related to their combination of unusual characteristics, such as extraordinary mechanical properties, low density, high surface area, biocompatibility, biodegradability, and sustainability (Dufresne 2013; Klemm et al. 2018). Its application thus expands from the production of plastic and paper, acting as a strengthening additive (Klemm et al. 2018), a rheology modifier in coatings (Klemm et al. 2018) or deposits (Hubbe et al. 2017), up to the production of functional nanoengineered materials for forthcoming cutting-edge applications in electronics (Abitbol et al. 2016), energy storage (Kim et al. 2019; Beeran et al.

2016), electromagnetic interference shielding (Gopakumar et al. 2018; Zeng et al. 2020), solar cells (Du et al. 2017), and photo/catalysis (Kaushik and Moores 2016) by acting as a template or carrier of carbon nanotubes (Miyashiro et al. 2020), graphene (Beeran et al. 2016; Wicklein et al. 2014), and metal oxides (Oun et al. 2020; Kaushik and Moores 2016), thus generating products with high optical transparency, good thermal stability and low heat transmission.

However, toxicological concerns and ecological acceptability of such hybrid materials during and after use are also becoming increasingly important. Many recent studies have, thus, focused on the application of nanoparticles based on silicon (Mastalska-Popławska et al. 2017; Li et al. 2017; Lin et al. 2018), minerals (montmorillonite (Köklükaya et al. 2017), carbonate (Farooq et al. 2018), kaolinite (Castro et al. 2018), hydroxyapatite (Guo et al. 2018), sepiolite (Ghanadpour et al. 2018)), magnesium derivatives (Jiang et al. 2019), or their combinations (Köklükaya et al. 2017; Wang et al. 2018; Li et al. 2017). Among them, aluminum hydroxide based nanoparticles are becoming one of the cheapest, easy-to-obtain and well-processable alternatives, which exist in various compositions and morphological crystal structures, depending on the synthesis routes (He et al. 2018). While aluminum trihydroxyde ($Al(OH)_3$ / ATH) can exist in four polymorphs, among which gibbsite is the most relevant, followed by three much rarer forms of bayerite, doyleite and nordstrandit, the aluminum monohydroxide (AlO(OH) / AMH), known as boehmite, has well crystallized orthorhombic unit cells (Karger-Kocsis and Lendvai 2018). All structures act in the condensed phase, where they decompose endothermically (between 180 and 200 °C and 400–700 °C, respectively) (Laoutid et al. 2009), thus absorbing 594 kJ/mol and 257 kJ/mol of energy/heat (Karger-Kocsis and Lendvai 2018), and forming aluminum oxide (Al_2O_3), together with the release of water molecules, according to Eqs. 1 and 2:

$$2Al(OH)_3 \rightarrow Al_2O_3 + 3H_2O \quad (1)$$

$$2AlO(OH) \rightarrow Al_2O_3 + 2H_2O \quad (2)$$

The thus diluted combustible gases reduce the burning temperature and prevent the access of oxygen by formation of a protective ceramic or vitreous layer on the surface from the residual crystalline polymorphic phase of Al_2O_3, thus improving its thermal stability (Hull et al. 2011; Laoutid et al. 2009). The effect of both particles‘ thermal stability is increased by decreasing the particle size (He et al. 2018) and increasing its concentration (Hull et al. 2011) and dispersibility (Norouzi et al. 2015). However, this influences the product‘s mechanical properties and transparency (Beyer 2001). In addition, the abundant surface decorated peripheral OH functional groups offer good dispersion and filler/matrix adhesion properties, especially when being prepared with a cellulose. However, the rare, and mostly recently published studies, based solely on the use of ATH particles as flame retardants for production of transparent cellulose based composite films (Zhang et al. 2017; He et al. 2018) or aerogels (Gorgieva et al. 2020; Yuan et al. 2016), that at 10–66 wt% of loading increase the products‘ residue between 10% and 46% at 600 °C and decrease the flammability, arehighly dependent on the type of cellulose used (nanofibrils, fibers or surface-functionalized polymer) and co-additives (such as sodium silicate, Gorgieva et al. 2020). The only study we found based on the use of AMH, was performed in combination with a bacterial nanocellulose by De Salvi et al. (2012); the film residue increased by up to 42% with the addition of 500 wt% of AMH, but its mechanical properties were reduced significantly.

The aim of the presented work was, thus, to examine the effect of structurally different aluminum hydroxide nanoparticles (prepared as tri or mono hydrated alumina, $Al(OH)_3$ vs. AlO(OH)), their dispersibility and loading quantity on the optical, mechanical, thermal and heat transmission properties of the films prepared from microfibrillated cellulose (MFC), in order to define their limitation in heat resistant applications such as flexible electronics. The films' wetting and oxygen permeability were also examined, to define their application potential in thermosensitive packaging.

Experimental

Materials used

1.9 wt% water suspended wood-based microfibrillated cellulose (MFC, Exilva F-01-L, Borregaard AS, Norway), consisting of 22–50 µm long and up to

100 nm tight fibrils with negative surface charge of -28 ± 2.2 mV and 18.5 ± 4.0 mmol/kg, as determined by using conductometric titration, were used throughout the study. The 16–21 μm sized $Al(OH)_3$ particles were purchased from Kemipal-W 900, Kemira KTM, Slovenia. Aluminum isopropoxide (Al(O-i-Pr)3), 2-propanol, acetic acid, 2-octanol, and polyethylene glycol 400 were purchased from Sigma-Aldrich, USA. Dolapix ET 85 (the dispersing agent) was obtained from Zschimmer and Schwarz Inc, Germany).

Preparation of nanoparticles

Aluminum trihydroxide (ATH, $Al(OH)_3$) nanoparticles were prepared from commercially available micro-sized $Al(OH)_3$ particles by the two-stage grinding process. For 40 nm average-sized ATH (designated as ATH40) particles' preparation, distilled water, commercially bought $Al(OH)_3$ and polyethylene glycol as a dispersant were weighed into an agate grinding bowl from the Planetary Mill (Pulverisette 5 classic line, FRITSCH GmbH, Germany) in the mass ratio of 1: 1: 0.35, and ground for 60 min at 280 rpm with grinding balls (Yttria-stabilized zirconia, Yotai Refractories Co. Ltd, Japan) of 2 mm in diameter. The grinding balls were then replaced with ones having a diameter of 0.5 mm, and 2-octanol (as an antifoaming agent) was added to grind the particles for another 60 min at 320 rpm. For the preparation of 50 nm average-sized ATH (ATH50) particles, the antifoaming agent (2-octanol) and deflocculant (carboxylic acid ester, Dolapix ET 85) were added at the first stage of grinding, followed by the second stage as described above for the preparation of ATH40 nanoparticles.

Aluminum monohydroxide (AMH, AlO(OH)) particles were prepared by the sol–gel procedure according to our previous study (Bunderšek et al. 2016). Briefly, aluminum isopropoxide ($Al(O\text{-}i\text{-}Pr)_3$) was added to 2-propanol as a carrier mediium and stirred. The mixture was then heated to about 82 °C, the boiling point of 2-propanol, and then refluxed to become a clear slurry. Acetic acid, as a catalyst, and distilled water, were added to the slurry to perform hydrolysis. The mol ratio of reactants of $Al(O\text{-}i\text{-}Pr)_3$: 2-propanol: acetic acid: water was 1: 25: 0.1: 6. The reaction was kept at temperature for 60 min to produce the amorphous AMHs. The AMHs were then peptized and crystallized by refluxing for 20 h. Distilled water was added at room temperature (20 °C) to obtain 20 nm sized particles (AMH20), where, for the 30 nm sized ones, the distilled water was heated to 40 °C (AMH30).

All the particles were washed fully with distilled waterafter preparation, and used as such for film preparation, or being air-dried for specific analysis.

Preparation of the films

The films' preparation process is presented schematically in Fig. 3. The 1.9 wt% water suspended MFC was first diluted by distilled water to 0.3 wt% suspension, and homogenized for 4 min with an Ultra Turax at 10,000 rpm. To such prepared MFC suspension, different weights of never-dried water-suspended ATH/AMH nanoparticles were added, by mixing them for 15 min with a magnetic stirrer at 1200 rpm, thus yielding final ATH/AMH mixture contents of 0.03 wt%, 0.09 wt% and 0.15 wt%, respectively. 50 ml of each dispersion was poured onto a Petri dish and air-dried at room temperature until the film was formed. The maximum amount of ATH/AMH nanoparticles' addition to MFC was chosen according to their film-forming ability. A sample prepared from MFC without nanoparticles was used as a reference. The composite films were designated according to the amount and type of ATH/AMH nanoparticles added, where the first number (1, 2 or 3) denotes the weight percentage of ATH/AMH particles' addition (1–0.03 wt%, 2–0.09 wt% and 3–0.15 wt%), and the second their average size (20 nm, 30 nm, 40 nm or 50 nm). For example, MFC-3-AMH20 means 0.3 wt% MFC with 0.15 wt% added AMH nanoparticles of average size of 20 nm.

Characterization of nanoparticles

X-Ray Diffraction (XRD; Miniflex II, Rigaku Corporation, Tokyo, Japan) was used to examine the crystallographic structures. The Dynamic Light Scattering (DLS) technique (Horiba LB 550, Japan) was used to determine the average size of the particles. The Specific Surface Area (SSA) was measured with a Surface Area and Porosity Analyzer (Micrometrics Tristar 3000, Micromeritics, Norcross, GA, USA) by using nitrogen adsorption–desorption and a Brunauer–Emmett–Telle (BET) model, where SSA was determined by calculating the amount of absorbed nitrogen gas, corresponding to a monomolecular layer of

nitrogen on the surface of the sample, and consideration of the nitrogen SSA (0.162 nm^2) as a function of relative pressure; the samples were dried before analyses (HG63, Mettler Toledo) at 105 °C for 60 min.

The morphology and elementary structure of the air-dried particles was characterized by using a Scanning Electron Microscope (SEM), Sirion 400NC (FEI, USA), equipped with an Energy-Dispersive X-ray spectroscope, INCA 350 (Oxford Instruments, UK). In addition, a probe Cs-corrected Scanning Transmission Electron Microscope (STEM) JEOL ARM 200F equipped with a cold field emission electron source, was applied to image the never-dried and in ethanol diluted particles. To minimize radiation damage, an 80 kV accelerating voltage and low beam currents were used. Powder samples were transferred directly to Lacey carbon-coated nickel TEM grids, while the suspensions were first diluted with ethanol, and a drop of the diluted suspension was placed on the grid.

The Thermo-Gravimetric Analysis (TGA) was conducted using a DSC1 analyzer, (Mettler Toledo, Switzerland), and Differential Scanning Calorimetry (DSC) was performed using a DSC823e Module STARe System (Mettler Toledo, Switzerland). Aluminum pans with pierced lids, containing $\sim$ 40 mg of sample for TGA analysis and $\sim$ 22 mg of sample for DSC analysis, were taken for analyzing the samples in an air atmosphere with a temperature rate increase of 10 °C/min from 25 °C to 600 °C. One measurement per sample was conducted for all of the above analyses.

Characterization of the films

SEM imaging of the films was performed to study the morphology and nanoparticle distribution.

Fourier Transform Infrared (FTIR) spectra of the films were recorded by using a Perkin-Elmer Spectrum One spectrometer (US). The transmission measurements were carried out in the range of 400–4000 cm^{-1} with 16 scans and a resolution of 4.0 with intervals of 1 cm^{-1}. The Spectrum 5.0.2 software program (version 10.6.1.) was applied for the data analysis. One measurement was made per film.

The transmission vs. reflection of the films was recorded within the 250–750 nm wavebands by using a Lambda 900 UV–Vis spectrophotometer (Perkin Elmer, USA) with an integrating sphere and scanning speed of 450 nm min^{-1}. One measurement was made per film.

Contact Angle (CA) measurements of the films were performed using an SCA20 Contact Angle measurement system (Goniometer OCA 35, Dataphysics, Germany). All measurements were conducted at room temperature on both sides of the films, with milliQ water used as the test liquid, volume of 3 mL. Each CA value was the average of six drops of liquid per surface, where three measurements were made for each side of the film.

The oxygen permeability of the films was measured using a Perme OX2/230 Oxygen Transmission Rate Test System (Germany), and the results evaluated by the software program WinPerme OX2-230 W3-330. All measurements were conducted at a temperature of 23 $\pm$ 0.1 °C and 50 $\pm$ 1% humidity. Four measurements were performed for each tested sample.

The tensile strength properties of the films were performed using a Shimadzu AGS-X electromechanical universal testing machine (Japan) according to the Standard ISO 6892–1:2009(E). The (55 mm long) samples were cut into a paddle shape (10 mm width of the wide part and 15 mm length of the wide part – on each side, with 3 mm width of the narrow part in the middle and 19 mm length of the narrow part), attached to clamps at a distance of 30.8 mm and tested at a speed of 0.05 mm/s. Three measurements were performed for each sample.

Thermo-Gravimetric Analysis (TGA) and Dynamic Scanning Calorimetry (DSC) measurements of the films were performed using a Mettler-Toledo DSC1 instrument (Switzerland) under air atmosphere in a temperature range from 25 to 600 °C and the heating rate of 10 °C/min, using a 50 mL/min flow rate. For TGA analysis a 150 µL platinum crucible was used, and the initial mass of samples (4–5 mg) being cut with scissors to suitable dimensions. The blank curve was subtracted in all measurements. For DSC measurements, the samples (0.5–1.0 mg), weighed carefully in a 20 µL light aluminum pan on an external Mettler Toledo MX5 balance, were pressed to the bottom of the crucible with a Teflon rod with a pierced lid, to provide contact during all the measurements and, thus, prevent the undesirable loss of the DSC signal. An empty aluminum pan served as a reference. One measurement was made per film.

Quasi-static specific Heat Capacity was studied by a new temperature modulated DSC technique—TOPEM, introduced by Mettler-Toledo, using a Mettler Toledo DSC1 instrument (Switzerland) (Schawe et al. 2006). The measurements were performed under multi-frequency temperature-modulated conditions in a temperature range from 20 °C to 240 °C, and heating rate of 1 °C/min, and a modulation amplitude of ± 0.5 °C. Samples with initial masses from 2 to 3 mg (approx. 5 stacks of a round-cut film) were placed into a 20 µL aluminum crucible and covered with a lid, which was pressed down firmly with a Teflon rod. An empty crucible served as a reference. One measurement was made per film.

Results and discussion

Structural, morphological and thermal properties of synthesized nanoparticles

The structure and thermal properties of the prepared ATH/AMH nanoparticles were evaluated using different analytical techniques.

The SEM and STEM images, presented in Fig. 1a and b, show agglomerated and different morphological features of the synthesized nanoparticles: Uniformly distributed and mostly plate/flat structured ATHs and smaller spherical shaped AMHs aggregates. The XRD diffractograms (Fig. 1c) indicated that the ATH particles had a mixed crystal phase of predominantly monocline gibbsite ($Al(OH)_3$) and meta-stable orthorhombic boehmite (AlO(OH)) (Reddy et al. 2014), being reflected in the well-defined narrow sharp peaks between 18° and 22° and some broader peaks at higher 2-theta (JCPDS No. 33–0018), respectively. On the other hand, weak broad peaks between 10° and 30°, characteristic for the boehmite (AlO(OH)), and the two sharp reflections at around 37° and 44° with a small shoulder at around 66°, characteristic for bayerite (Al_2O_3), were indicated for the AMH particles, as already confirmed by our previous study (Bunderšek 2015; Bunderšek et al. 2016). The difference in the crystalline structure is supported by the elemental compositions (Table 1), that confirmed the presence of different weight mass of oxygen and aluminum, as well as the formation of hybrid structures with different O/Al ratios (i.e. 1.27 for AMH20 and 1.90 for ATH40). DLS (Fig. 1d) and BET (Fig. 1e, Table 1) analysis indicated that the ATH particles were much larger (∼ 39.6 nm / ATH40 and ∼ 49.7 nm / ATH50), with an SSA of 18.9 m^2/g and 59.5 m^2/g, respectively, compared to the AMH particles (AMH20 and AMH30), being in the range of 21.7–31.9 nm, and possessing much higher, but comparatively similar SSA (385.4 m^2/g and 377.7 m^2/g). The slightly lower SSA of ATH40 than ATH50 might be due to their higher tendency to agglomeration.

According to the nitrogen adsorption–desorption isotherms (Fig. 1e), the pore diameter of the ATH samples is in the range of 14.9–15.9 nm and AMH based around 6.7 nm, which means that the pores of both types of particles are classified as mesopores (range 2–50 nm) (Sing 1985). The nitrogen adsorption–desorption hysteresis loop performed on the samples showed a type IV isotherm, which is associated with capillary condensation taking place in the mesopores. However, there was a big difference between the steepness and width of the isotherms for the ATH *vs.* AMH particles. The hysteresis loop of the ATH based samples was very steep, almost vertical, which points to agglomerates or spherical particles arranged in a uniform way, and facile pore connectivity. On the other hand, the AMH samples had a wider and more gradual slope, indicating aggregates and slit shaped pores with good connectivity.

The thermal properties of the synthesized ATH/AMH nanoparticles, evaluated by thermal decomposition in an air atmosphere between 25 °C and 600 °C (Fig. 2d), indicated that the amount of residue at 600 °C for both types of nanoparticles were almost the same (from 65.4% to 69.5%). However, thermal degradation of AMHs occurs in two steps, while ATH ones in one step, where most of the weight loss (29%) occurs in the range of 250–320 °C, attributed to the transformation from $Al(OH)_3$ to Al_2O_3 according to Eq. 1, or via AlO(OH) (Favaro et al. 2010; Lamouri et al. 2017), and, up to 600 °C, an additional 5% of weight is lost. On the other hand, the AMH particles start to degrade soon after the temperature is increased, resulting in a weight loss of 14.1% (AMH20)—18.2% (AMH30) in the range of 25–200 °C, due to topotactic transformation of the meta-stable boehmite phase (release of one mole of water; Karger-Kocsis and Lendvai 2018), while only 7% of additional weight is lost in the range of 200–400 °C, and an additional 9% up to 600 °C,

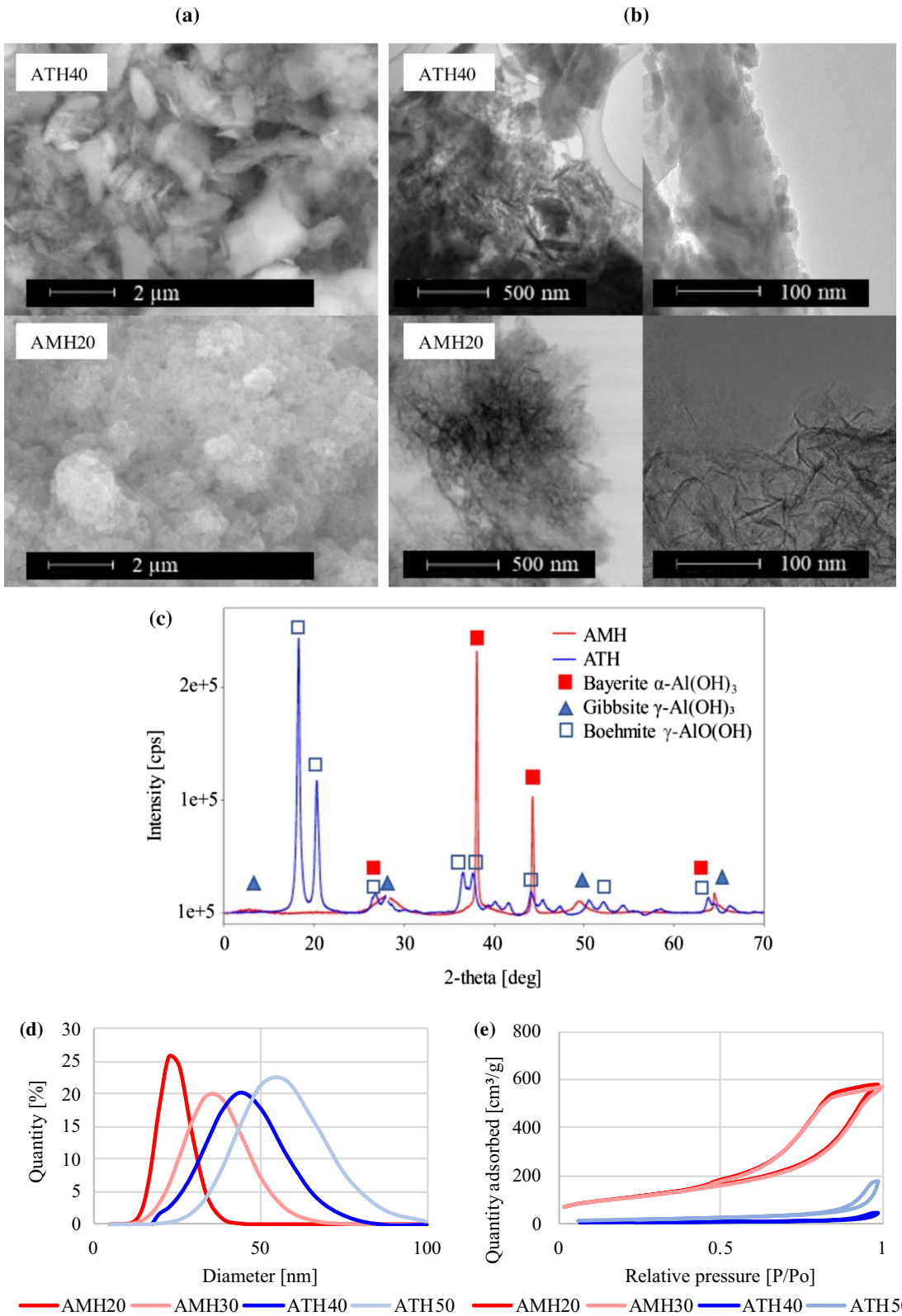
(a)
(b)
ATH40
2 µm
ATH40
500 nm
100 nm
AMH20
2 µm
AMH20
500 nm
100 nm
(c)
AMH
ATH
Bayerite α-Al(OH)3
Gibbsite γ-Al(OH)3
Boehmite γ-AlO(OH)
Intensity [cps]
2e+5
1e+5
1e+5
0
20
30
40
50
60
70
2-theta [deg]
(d)
Quantity [%]
30
25
20
15
10
5
0
0
50
100
Diameter [nm]
AMH20
AMH30
ATH40
ATH50
(e)
Quantity adsorbed [cm³/g]
800
600
400
200
0
0
0.5
1
Relative pressure [P/Po]
AMH20
AMH30
ATH40
ATH50

◀**Fig. 1** **a** SEM and **b** TEM images, **c** XRD patterns, **d** Size distribution curves measured by DLS, and **e** BET_N adsorption–desorption isotherms of differently prepared ATH/AMH nanoparticles

indicating its gradual change into nanocrystalline Al_2O_3 forms with smoother, but still different, morphological structure (Fig. 2a and b). When exposed to elevated temperatures, all types of tri/mono-hydrated alumina nanoparticles thus transform to γ-Al_2O_3, which is shown with almost equal XRD diffractograms (the main characteristic peaks at around 38°, 45° and 67°; Sifontes et al. 2014; Rahmanpour et al. 2012; Fig. 2c), as well as similar elemental compositions (Table 1), but slightly different O/Al ratio (1.14 vs. 1.26), which might be due to the different kinetic of transformation and formation of structurally different polymorphs of alumina; the gibbsite ($Al(OH)_3$) in the transformation sequence firstly transits to boehmite (AlO(OH)), and, in the next phase, to γ-Al_2O_3. Boehmite, on the other hand, needs to undergo one phase less (Favaro et al. 2010), therefore, larger compositional changes are present in the transformation of $Al(OH)_3$, leaving a larger difference in the O/Al ratio. The slower degradation rate of AMH particles at higher temperatures, meaning also better thermal stability, which can also be reflected from the DSC analysis (Fig. 2e) and calculated relevant enthalpy values, are collected in Table 1.

According to the different path and mode of thermal transformation (Eqs. 1 and 2), much more energy is, thus, released during the decomposition of ATH nanoparticles (876.4 J/g for ATH40 and 752 J/g for ATH50) as compared to the AMH ones (245.3 J/g for AMH20 and 232.2 J/g for AMH30). The smaller and nanocrystalline-structured AMH particles with numerous H-bonding and internally adsorbed water molecules, thus release less energy to transform in the minority present boehmite (AlO(OH)) structures, and further into the fully dehydrated Al_2O_3 forms, where, on the contrary, ATH particles need much more energy to be transformed from the predominant gibbsite ($Al(OH)_3$).

Surface morphological and physico-chemical properties of the films

The surface morphology and physico-chemical properties of the nanocomposite films were studied by SEM imaging, Contact Angle measurements, FTIR and UV–Vis spectroscopy.

A fibrillated and ribbon shaped structure is seen from the SEM imaging (Fig. 3a) for the pure MFC film, which is preserved even with the addition of the highest percentage (0.15 wt%) of ATH/AMH nanoparticles, but, however, gives differently distributed and dense films. Slightly aggregated, but uniformly and individually distributed ~ 40 nm large ATH nanoparticles, can be observed through the entire film (Fig. 3b), interacting well with the rare

Table 1 Structural and thermal properties of different ATH/AMH nanoparticles

Particle designation	ATH40	ATH50	AMH20	AMH30
Average size [nm]	39.6 ± 1.3	49.7 ± 1.3	21.7 ± 1.2	31.9 ± 1.3
Specific surface area [m^2/g]	18.9 ± 0.04	59.5 ± 0.15	385.4 ± 2.6	377.7 ± 2.1
Pore diameter [nm]	14.9	15.9	6.7	6.7
Pore volume [cm^3/g]	0.07	0.28	0.91	0.89
Weight loss 25–100 °C [%]	0.6	0	14.1	18.2
Additional weight loss 200–400 °C [%]	29.9	29.5	7.3	7.6
Residue at 600 °C [%]	67	67.5	69.5	65.4
Enthalpy [J/g]	−876.4	−752.9	−245.3	−235.2
Al [wt%]	34.39 ± 1.3	n.d	43.94 ± 3.1	n.d
O [wt%]	65.61 ± 1.3		56.06 ± 3.1	
O/Al	1.908		1.276	
O/Al at 600 °C	1.142		1.261	

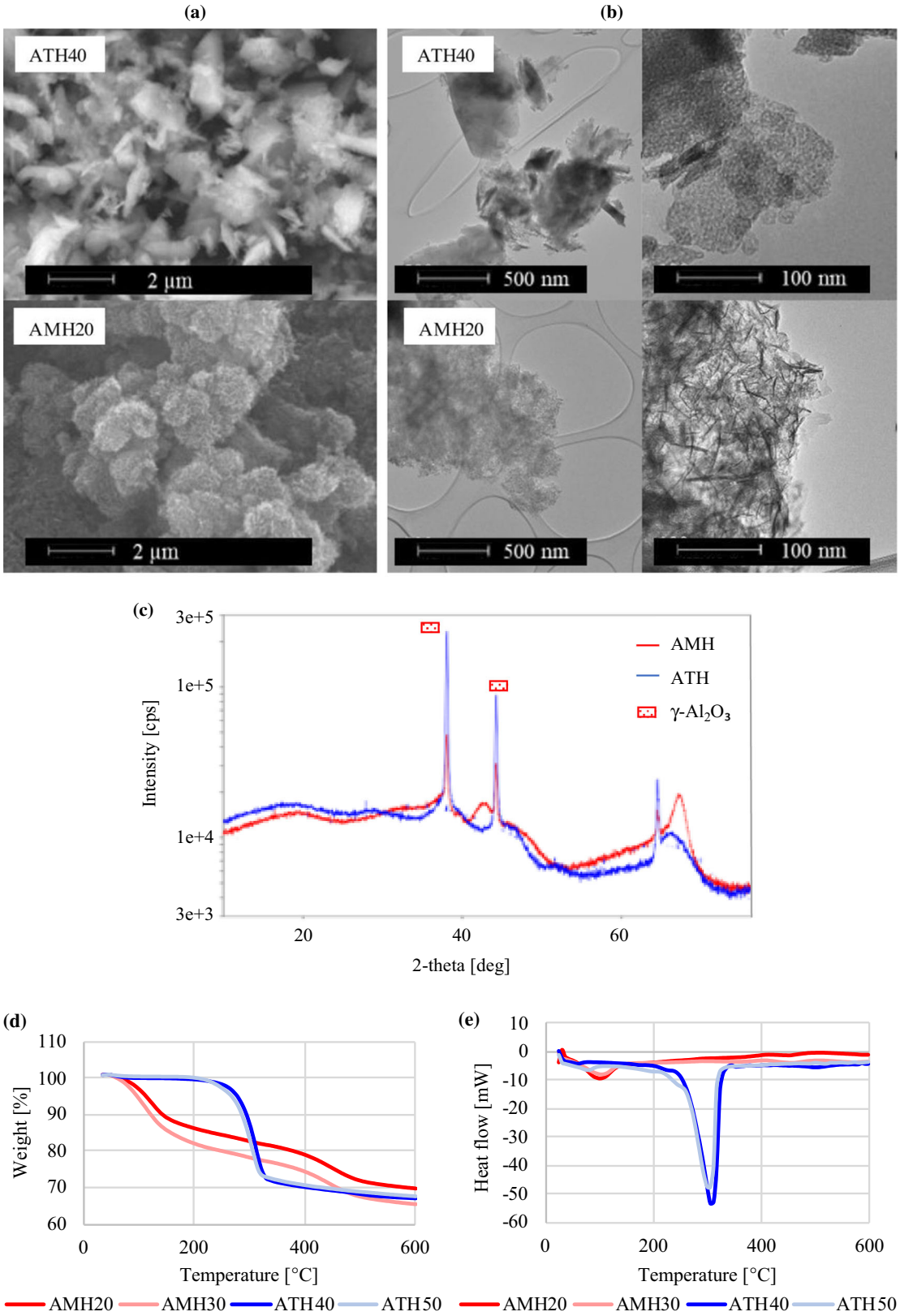
(a)
(b)
ATH40
2 µm
ATH40
500 nm
100 nm
AMH20
2 µm
AMH20
500 nm
100 nm
(c)
3e+5
1e+5
1e+4
3e+3
Intensity [cps]
20
40
60
2-theta [deg]
AMH
ATH
γ-Al2O3
(d)
110
100
90
80
70
60
Weight [%]
0
200
400
600
Temperature [°C]
AMH20
AMH30
ATH40
ATH50
(e)
10
0
-10
-20
-30
-40
-50
-60
Heat flow [mW]
0
200
400
600
Temperature [°C]
AMH20
AMH30
ATH40
ATH50

◀**Fig. 2** **a** SEM and **b** TEM images, **c** XRD analysis of ATH/AMH nanoparticles after thermal degradation at 600 °C, **d** TGA and **e** DSC analysis of differently prepared ATH/AMH nanoparticles

negative surface charge and huge -OH groups of cellulose backbone, and, thus, covering the surface of the cellulose fibrils fully. On the other hand, the areas of denser cellulose fibrillar net structures were observed, containing well dispersed ~ 20 nm large AMH particles with intermediate free spaces (Fig. 3c). Such an effect might be due to the use of the faster volatile 2-propanol as a dispersing media for AMH particles, which induced attractive interactions between the fibril's -OH groups, acting as a glue, and, thus, inducing phase separations between the water-rich (98.3%) and alcohol-rich (17.9%) gelation regions of the cellulose microfibrils (da Silva et al. 2018), yielding nanostructured and inhomogeneous clustering of microdomains of the MFC containing AMH particles. Optionally, AMH particles consisting of two double layers of aluminum centered distorted octahedra $AlO_4(OH)_2$ forms, may also get separated by the hydrogen bond interaction between the AlO(OH) inter-layer OH and cellulose –OH groups after mixing (De Salvi et al. 2012), and exfoliate on the fibrils' surface during drying.

FTIR spectra of MFC-based films containing 0.15 wt% of ATH/AMH particles (ATH40, AMH20) are presented in Fig. 4, and compared with those of pure MFC film to confirm the interactions between the components. The FTIR spectra of ATH40 particles show typical four mode peaks over the range of 3620–3380 cm^{-1}, being related to the stretching of OH groups that are interacting with the Al atoms (He et al. 2018), and being supported by Al–O stretching at ~ 1020 cm^{-1} (Gorgieva et al. 2020), corresponding to the predominant $Al(OH)_3$ structure. On the other hand, AMH20 has a much larger and broader peak for asymmetric and symmetric OH stretching vibrations, centered at ~ 3300 with a small shoulder at ~ 2900 cm^{-1}. Absorption bands appeared at ~ 1637 cm^{-1} (assigned to the stretching and bending modes of the adsorbed water molecules), as well as a string band at ~ 1065 cm^{-1} with a small shoulder at ~ 1160 cm^{-1} (assigned to the bending and wagging of the H bonds in the octahedral structure of OH-Al = O), at ~ 746 cm^{-1} (attributed to the stretching vibrations of Al–O–Al in the distorted AlO_6), at ~ 664 cm^{-1} and ~ 559 cm^{-1}, all consistent with the reported values for a boehmite AlO(OH) structure (Abdollahifar et al. 2018) and the crystalline structures of Al_2O_3 as defined by XRD analysis (Fig. 1c). The peaks which appeared at ~ 1550 cm^{-1} and ~ 1420 cm^{-1} for AMH20 could be the remains of the aluminum isopropoxide (Herreros and Klinowski 1995; Kamal 2008) and/or acetic acid (Hasan et al. 2003) used in the synthesis process.

The FTIR spectrum of pure MFC film shows typical cellulose bands: A broad band at ~ 3323 cm^{-1} for hydrogen bonded OH stretching, at ~ 2892 cm^{-1} for CH stretching, at ~ 1640 cm^{-1} for OH bending of absorbed water, at ~ 1420 cm^{-1} for CH_2 bending, at ~ 1026 cm^{-1} for C-O bending, and at ~ 897 cm^{-1} for CH or CH_2 stretching (Lu et al. 2008; Gorgieva et al. 2020). The presence of ATH40 in the MFC intensified its peak related to the OH groups over the range of 3616–3349 cm^{-1}, also showing three shoulders typical for Al–OH interactions on its backbone, as well as a characteristic peak for Al–O stretching of ATH40 at ~ 1018 cm^{-1} (Gorgieva et al. 2020). This may indicate the hydrogen bonding between the –OH groups of ATH particles and the cellulose backbone of MFC, covering the fibrils' surfaces. All the mentioned OH related peaks (in the range of 3600–3300 cm^{-1}) are not present on a broader and much smaller band, shifted to ~ 3314 cm^{-1} in the case of MFC–AMH20 based film, on which bands characteristic for AMH20 are overlapping with those typical for cellulose structures, so they cannot be distinguished in the spectra. However, the hydrogen bond interactions between the –OH groups of MFC and–OH groups of AlO(OH) nanoparticles or oxygen of Al_2O_3, as well as between the ATH particles themselves, resulting in the presence of Al–O, according to the separation mechanism of octahedra $AlO_4(OH)_2$ forms as described above.

To support the finding of the chemical composition and topology of the films' surfaces, the wetting properties of the films were evaluated by measuring the Contact Angles (CA) using milliQ water. A larger CA indicates low surface energy and higher hydrophobicity (Wu et al. 2014). As seen from the results presented in Fig. 5, the addition of ATH/AMH nanoparticles to MFC changed its original CA value significantly (~ 43°), which is in the range for the other cellulose based films (from 28° (Andresen et al.

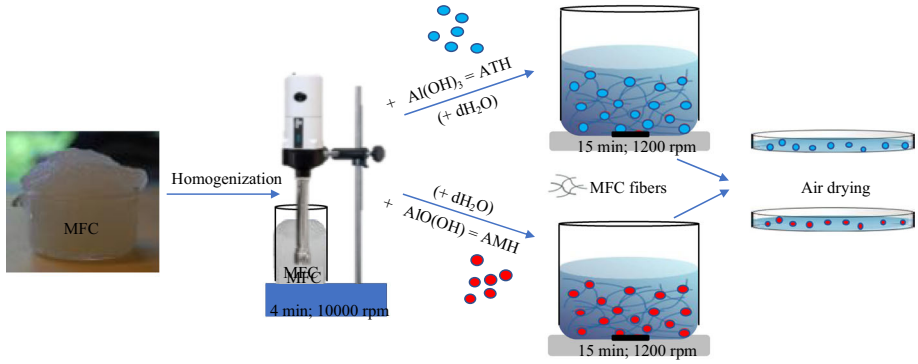
MFC
Homogenization
MFC
4 min; 10000 rpm
+ Al(OH)3 = ATH
(+ dH2O)
(+ dH2O)
+ AlO(OH) = AMH
15 min; 1200 rpm
MFC fibers
15 min; 1200 rpm
Air drying

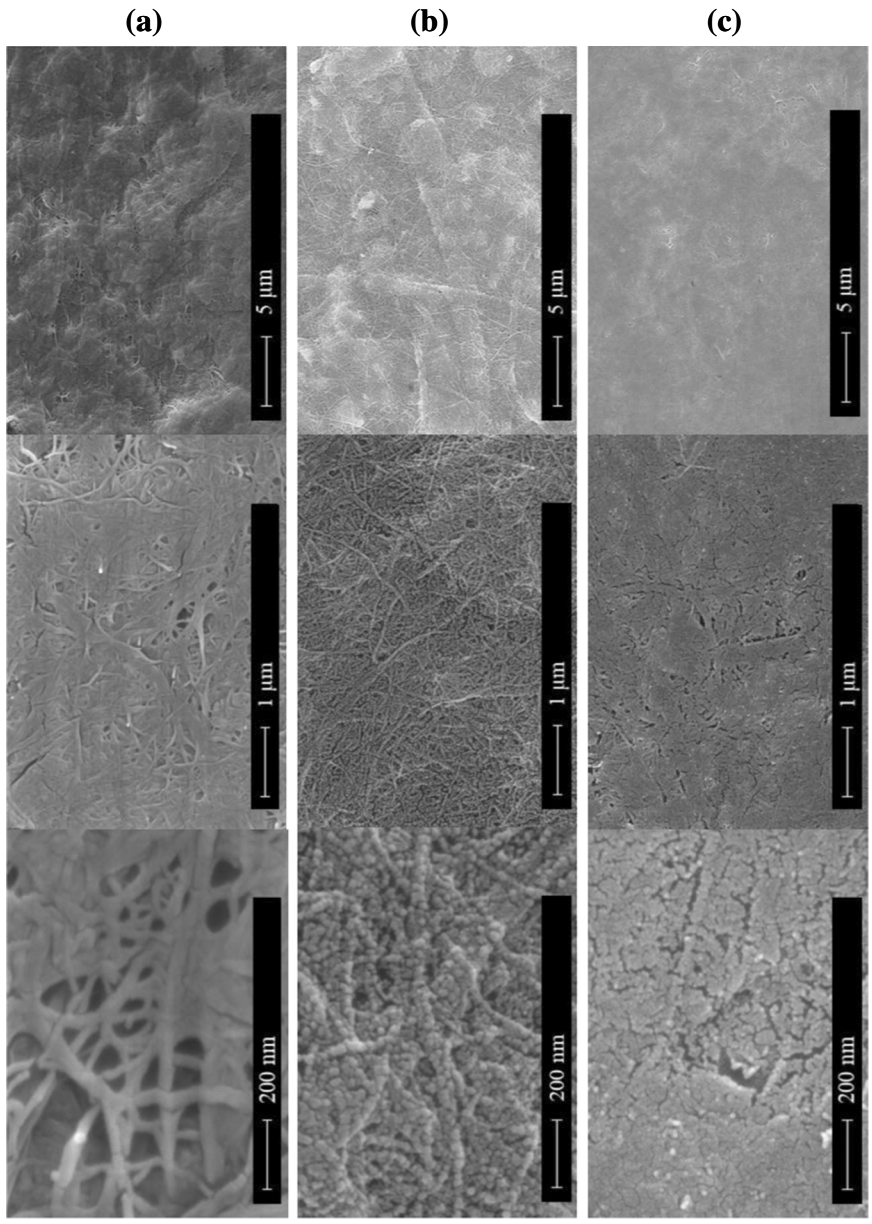
(a)
(b)
(c)
5 µm
1 µm
200 nm

◀**Fig. 3** Preparation protocol (upper), and SEM images (lower) of films prepared from **a** MFC, and MFC with the addition of 0.15 wt% of **b** ATH40 and **c** AMH20 nanoparticles

2006) to 60° (Belbekhouche et al. 2011)), confirming its high hydrophilicity due to the presence of the many OH groups on its surface. The addition of ATH40 and ATH50 to MFC additionally lowered the CA of such a film to around 32°-33° at the highest (0.15 wt%) concentrations, which might be due to the presence of additional highly hydrophilic -OH groups arising from the presence of ATH particles fully covering the cellulose fibrils, as confirmed with the FTIR spectra and SEM analysis. On the other hand, the CA was increased up to ∼ 68° for films prepared with 0.15 wt% of AMH20 and AMH30 particles, also being in agreement with their SEM and FTIR analyses (i.e. reduced –OH groups on the MFC-AMH microdomains). In addition, the volatile 2-propanol present in the AMH during film preparation, goes to the surface preferentially, and, consequently, lowers the surface energy, making it more hydrophobic (Ballal and Chapman 2013). It is also worth mentioning that when water droplets were dripped onto the surface of such films, the droplets spread around the surface, but did not soak into the surface totally, nor did they induce the films‘ dissolution due to the presence of water. A small difference in the mean CA values between both surfaces can be observed in the case of the MFC-AMH30 film, given ∼ 72° on the upper-side and ∼ 66° on the lower-side. This might be due to a difference in the film‘s surface roughness and smoothness of the formed MFC-AMH microdomains, as can be seen from the SEM images, where a rougher surface gives a higher CA than smoother ones due to the heterogeneous wetting being related to the formation of air compartments between the droplets and the surface (Beeran et al. 2016).

To get a better insight into the bulk nanostructure of such films, the optical properties and Oxygen Transmission Rate (OTR) were evaluated of the MFC films containing different contents of ATH/AMH nanoparticles. The transmittance values (Fig. 6) of pure and thinner (∼ 19.2 μm) MFC film were the highest, and almost constant within all the wavelength ranges (from 98.9% at 400 nm to 93.4% at 700 nm), indicating that the film was fully transparent. The addition of ATH/AMH nanoparticles reduced the transmittance and increased the thickness of the film, which is, however, highly dependent on the dispersibility, the crystalline structure and the size of the used particles (Acharya et al. 2018). With the formation of aggregates, particles get larger, and, consequently, scatter the light more than the original small particles. The transmittance reduction is, thus, significant for 21–28 μm thin MFC–ATH films (from about 86% to about 25–48% at 30 and 0.15 wt% of ATH addition, respectively), while its changing in the case of MFC–AMH films is much smaller (between 96.8 and 89.4%) compared to the pure MFC film, although they are thicker (23–32 μm) and more dependent on the particle size than on their content. The reason for such a difference could be in the different crystalline structure, morphologically larger (40–48 nm), lower SSA (18.9–59.5 m^2/g), aggregated and less uniform ATH nanoparticles than AMH ones (21–31 nm), with much higher SSA (385.4–377.7 m^2/g), which, consequently, blocks the light transmission (Sathish et al. 2015). This can also be supported by increasing the transmittance values by increasing the wavelength for both MFC-ATH films (from 47 to 35% at 400 nm to 59% and 49% at 700 nm for MFC films containing ATH40 and ATH50, respectively). As such, films are also more hydrophilic, adsorbing more moisture, and, with the presence of $Al(OH)_3$ form-based particles, in addition increases the volume of voids between the fibrils.

The OTR values of films thus also decreased from ∼ 6622 cm^3/m^2day for pure MFC film to ∼ 3600 cm^3/m^2day and ∼ 2190 cm^3/m^2day for MFC-3-AMH30 and MFC-3-AMH20, respectively, which is related primarily to the nanoparticles‘ addition and their structures, and, secondly, to the films‘ density and thicknesses; the films made with ATH nanoparticles are, namely, approximately 10 μm thicker than pure MFC film. When comparing the OTR values to other related studies, a great variety of results were obtained for pure MFC films, while no measurements are available for composites prepared with the ATH/AMHs. For example, a much lower OTR value was obtained by Radionova et al. (2013), where 44 μm thick film prepared from 0.1 wt% MFC suspension had the OTR of 3.7 cm^3/m^2day, while it was lowerd to ∼ 17 cm^3/m^2day, and, further, to 1.4–0.1.7 cm^3/m^2day for 30 μm (Syverud and Stenius (2009) and 25 μm thick films (Kumar et al. 2014), respectively. On the other hand, the OTR

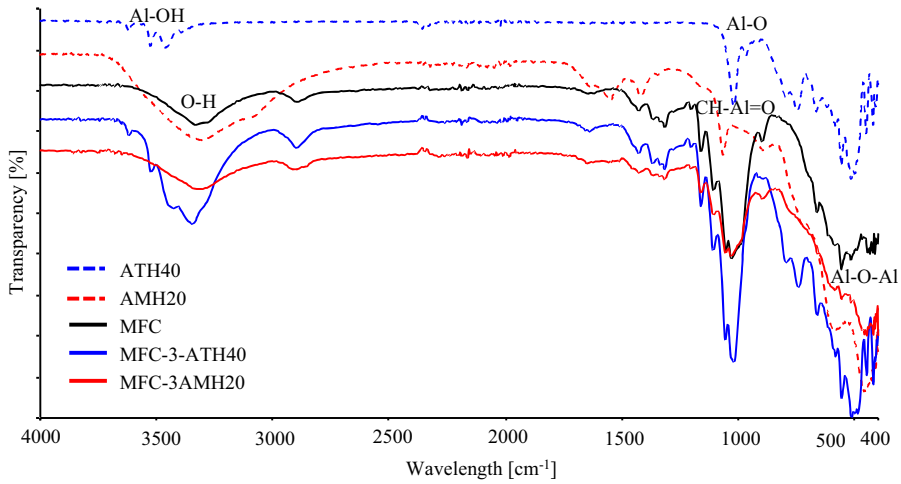

Fig. 4 FTIR spectrum of ATH40 and AMH20 nanoparticles and MFC films with and without the addition of 0.15 wt% nanoparticles

of ∼ 1447 cm^3/m^2day has been reported for 0.5 wt% based MFC film (Lyytikäinen et al. 2021).

Mechanical properties of the films

Tensile testing of the films was performed to identify the effect of type and content of nanoparticles' addition to MFC film by measuring the tensile strength and providing Young's modulus and elongation at break (Fig. 7). An increase of tensile strength up to 7.7–18.9% for the films containing up to 0.09 wt% addition of ATH nanoparticles, and its decrease by ∼ 3.7% by further increase of its content to 0.15 wt%, as compared to the pure MFC film (∼ 59.2 MPa), can be observed, with the elastic modulus following the same trend. On the other hand, a slightly different behavior was noticed for the films containing AMH particles. While a small reduction of both tensile strength (to ∼ 44–47 MPa, 20–25%) and Young's modulus (from 3.6 GPa to ∼ 2.8–3.3 GPa, 9–21%) were measured for the films containing the lowest (0.03 wt%) AMH content, as compared to the reference (pure MFC film), its increase to ∼ 69 MPa (17%) and ∼ 5.7 GPa (55%), respectively, by further addition of AMH20 (up to 0.15 wt%), but slight decrease (4.7 MPa / 19%) was obtained in the case of using AMH30. Elongation at break for all samples was lower than 5%, meaning that films are fractured before deforming under a tensile load. The MFC film's elongation at break was only slightly affected by the addition of ATH nanoparticles (it increased from ∼ 2% to ∼ 4% at 0.09wt% of ATH50 loading), while AMHs did not show an influence. The results support the previous findings, indicating the effect of ATH/AMH morphology, size and crystalline structure, which, altogether, contribute to (part or full), coverage

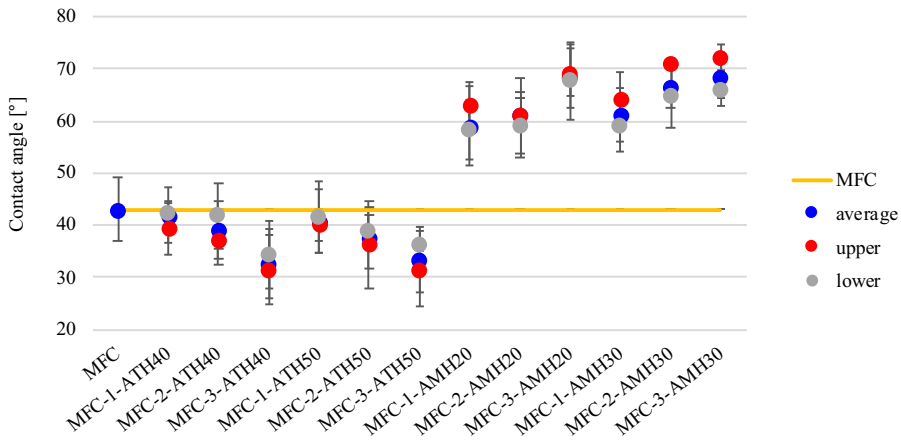

Fig. 5 Contact Angle values of different MFC-based films, measured on the upper / air-turned and lower / petri-turned sides

of cellulose fibrils' surfaces and result in differently nanostructured films. Smaller (∼ 21 nm) and well dispersed AMH20 particles with large surface area (385.4 m^2/g) thus result in more hydrogen bindings and dense connections inside the films.

Thermal stability of the films

Different techniques of TGA/DSC were used to evaluate the films' thermal properties in an air atmosphere and temperature range from 25 °C to 600 °C, including degradation temperature, residue amount after degradation, enthalpy and specific heat capacity.

As presented in Fig. 8a, thermal degradation of pure MFC occurs in three successive steps: From room temperature to approximately 230 °C, evaporation of physically adsorbed water takes place. In a temperature range from 230 °C to 350 °C weight loss is related to the collapse of the glucosidic structure and the formation of carbonyl compounds, which decompose completely at around 600 °C (Lichtenstein and Lavoine 2017). The addition of ATH/AMH nanoparticles changed the course of thermal decomposition of pure MFC, depending on the type used. About a ∼ 3.5% larger weight loss in the case of MFC-AMH20 films (∼ 6.6%) compared to the MFC-ATH40 ones, (∼ 2.9%) up to 200 °C was related to the different phase transformations of the used particles, as explained previously under the first Section. However, comparing the onset decomposition temperatures of the second step shows that MFC-AMH20 film (305 °C) was the most thermally stable, followed by pure MFC (281 °C) and MFC-ATH40 as the less stable (260 °C). The inflection point of both nanocomposite films occurred at around 330 °C, given a weight loss of around 60% in the case of MFC-ATH40, and around 40% for MFC-AMH20 films, while, for the pure MFC sample, this temperature was at around 350 °C with ∼ 59% of weight loss. The addition of ATH/AMH nanoparticles also had a noticeable effect on the amount of residue after thermal decomposition, which increased from ∼ 1.8% for pure MFC film to around 10% already with 0.09 wt% addition of ATH40

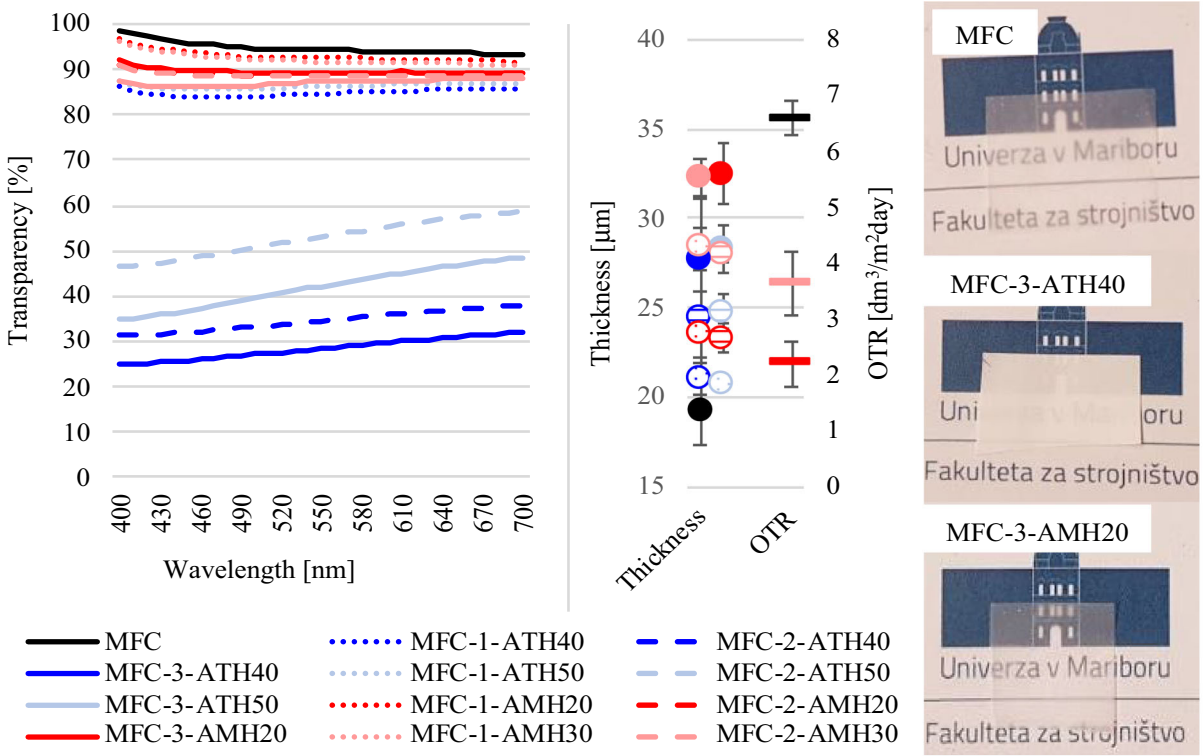

Fig. 6 Thickness, Transmittance and Oxygen Transmission Rate (OTR) values of different MFC-based films (left); photographic images of films showing their transparency (right) (use of the logotype is permitted by University of Maribor)

and AMH20, and further, to even ∼ 20–23% for films containing the highest (0.15 wt%) NP concentrations, which is comparable with the other cellulose based materials containing different ATH nanoparticles (Gorgieva et al. 2020; Zhang et al. 2017; Yang et al. 2017). The higher residue amount means that the ATH/AMH nanoparticles had suppressed the film' degradation successfully with the dilution of radicals in flame, while the residue of alumina formed the protective layer (Hull et al. 2011). Some additional differences during the films' thermal decomposition can be seen from the comparison of their derivative weight (DTG) curves (Fig. 8b). Decomposition of the films with incorporated ATH40 particles occurs via three steps; the first one from 230 °C to 280 °C, which occurs only in these samples. The DSC curves of these samples (Fig. 8c) show that this process is endothermic, being assigned to the dehydration of $Al(OH)_3$ and AlO(OH) structures. In the case of MFC films prepared with AMH20, the dehydration and thermal decomposition of the organic MFC matrix takes place simultaneously. It is also obvious from the DTG curves that the maximal rate of glucosidic degradation was faster when nanoparticles were added to the MFC, while the second step was much slower. Some relevant data about the thermal decomposition process of the studied samples are collected in Table 2. Shifted onset decomposition to higher temperature, weight loss at the inflection point and lower rate of decomposition in the second step, show that AMH20 films possess better thermal stability regarding the other MFC-ATH or pure MFC films.

In addition, the integrated values of the heat flow (Fig. 8c) show that the enthalpy of pure MFC film was reduced by about 57% (MFC-ATH40) and 42% (MFC-AMH20) (from ∼ 13,100 J/g to ∼ 5576 J/g and ∼ 7598 J/g, respectively), for the samples containing the highest (0.15 wt%) amount of nanoparticles. The decreased enthalpy values are related to less released energy in the process of burning, and, thus, its contribution to heating the film in the process of degradation was smaller. It is even more obvious from the comparison of DSC curves that the decomposition process differed as to whether AMH or ATH particles were added to the MFC. In the case of AMH particles, the shape of the DSC curves was similar to MFC, and the process was the most exothermic in the second step of decomposition. Besides the initial endothermic reaction at the beginning of thermal decomposition at 230 °C, already mentioned before, films with the addition of ATH released much more heat in the temperature region from 300 °C to 380 °C (the exception was the film prepared with the lowest ATH content, where it followed the MFC curve, meaning that 0.03 wt% ATH content was too low for making an observable difference). In the second step, much less heat was released compared to pure MFC and films prepared with the addition of AMH nanoparticles, where most of the released heat was present in the temperature range 400–500 °C. Such an effect might be due to the one step transformation from AlO(OH) to Al_2O_3 and simultaneous formation of protective char, compared to the $Al(OH)_3$ nanoparticles, which were transformed to Al_2O_3 with an additional phase change through the heating. In the process of films' decomposition, the ATH/AMH particles' shell created compact char structures that acted as heat insulators (Horrocks 2011). This reduced the thermal conductivity and the amount of released oxygen inside the material, and, due to the oxidation–reduction processes, it might absorb highly reactive radicals, which all inhibit thermal and mass flow inside the material, and, consequently, modify its course of degradation (Norouzi et al. 2015). This means that ATH/AMH nanoparticles can enhance the charring properties of the MFC matrix (He et al. 2018), and, by forming a protective layer over the MFC, protect it from further decomposition (Yuan et al. 2016).

The specific heat capacity of the prepared films was also evaluated to get information about their thermal isolation or heat transportation ability. Since heat capacity is the amount of heat required to change the temperature of one unit mass of material by one degree, and the heat capacity for any polymeric material is temperature dependent (Wen 2007), the heat capacities of the samples were measured up to 200 °C before the samples underwent the accelerated phase transitions. Heat capacities for polymers are usually in the range from 0 to 3 J/gK (Wen 2007), which also corresponds to that of our samples. The lower the heat capacity, the energy in the form of heat is transferred more easily through the film, thus cooling the material passively, and acting as a thermal conductor, that is becoming an emerging demand for, e.g., electronic products (Sato et al. 2020). As can be seen from the curves in Fig. 8d and specific heat capacity values collected in the inserted Table 2, the

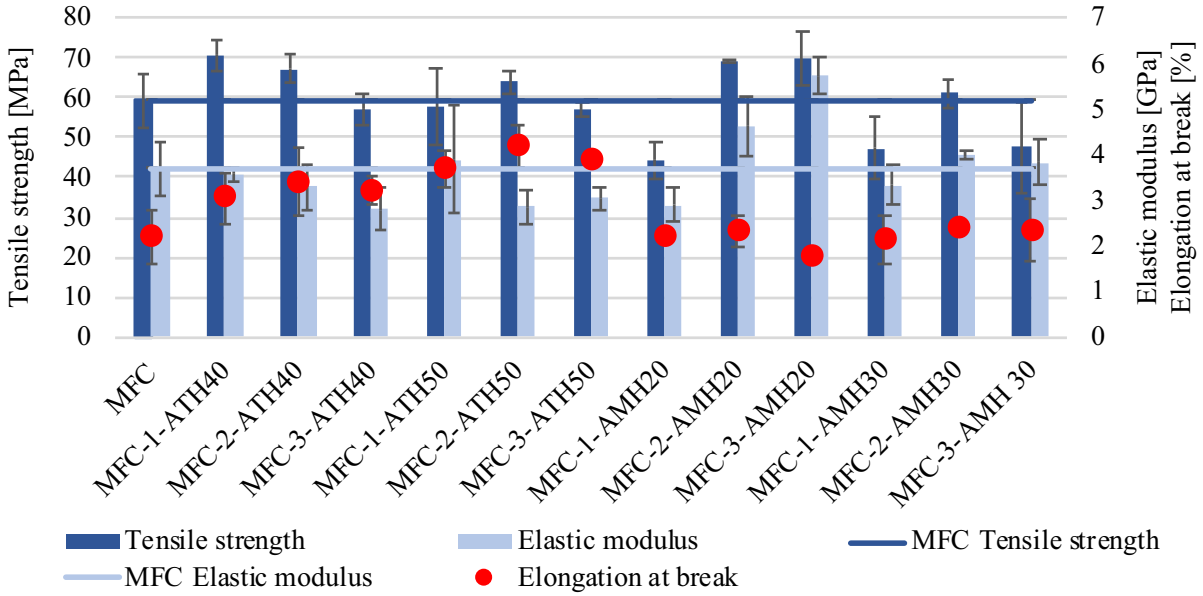

Fig. 7 Tensile strength, elastic modulus and elongation at break of different MFC-based films

values for all samples increased with increased temperature (an exception was the sample MFC-3-AMH20, where the values were almost constant), and decreased with the added amount of ATH/AMH nanoparticles, indicating their different insulation properties. The lowest heat capacity was observed for the highest concentration of AMH20 nanoparticles, where the value was reduced by more than ~ 65% compared to pure MFC film, which might be correlated to the dense and homogeneously covered cellulose fibrils with highly crystalline AlO(OH)/Al_2O_3 structured particles, which transferred the heat easily and evenly throughout the whole tested temperature region, thus acting as an efficient thermal remover by dissipating the heat. On the other hand, films prepared with more amorphous $Al(OH)_3$ based forms of ATH nanoparticles increased the heat capacity of the films up to ~ 57% compared to the pure MFC at lower ATH concentrations, and reduced it by around 22% at the highest content of larger ATH40, which might be related to the particles' aggregation. The aggregation of particles affects the thermal conductivity, where, with increased size of agglomeration, the interface between agglomerates is increased, and, consequently, leads to a reduction of thermal conductivity or decreased heat capacity (Machrafi et al. 2016). The improved heat transfer abilities of MFC–AMH films make them a good candidate for electronic products (Sato et al. 2020). Additionally, their lower OTR values and increased hydrophobicity also make them interesting for application in e.g., food packaged products. Packaging plays an important role in the protection of food products against a range of external influences, among which, besides oxygen and water–vapor barrier properties (Hubbe et al. 2017), temperature variations are becoming another issue that have a negative impact on keeping packaged foodstuffs fresh for longer durations (Singh et al. 2018).

Conclusion

Structurally and size-related different aluminum (tri/mono) hydroxide ($Al(OH)_3$ / AlO(OH)) nanoparticles were prepared, and used as a thermo-stable additive to thin-layered films of microfibrillated cellulose (MFC), to create new environmentally friendly and biodegradable materials. The addition of ATH/AMH nanoparticles increased the films' thermal stability significantly, as the residue amount after degradation got higher, degradation temperatures moved to higher values and the enthalpy was lowered. However, the films' optical, oxygen-barrier, mechanical, heat resistant and thermal-management properties were highly dependent on the particles' sizes and

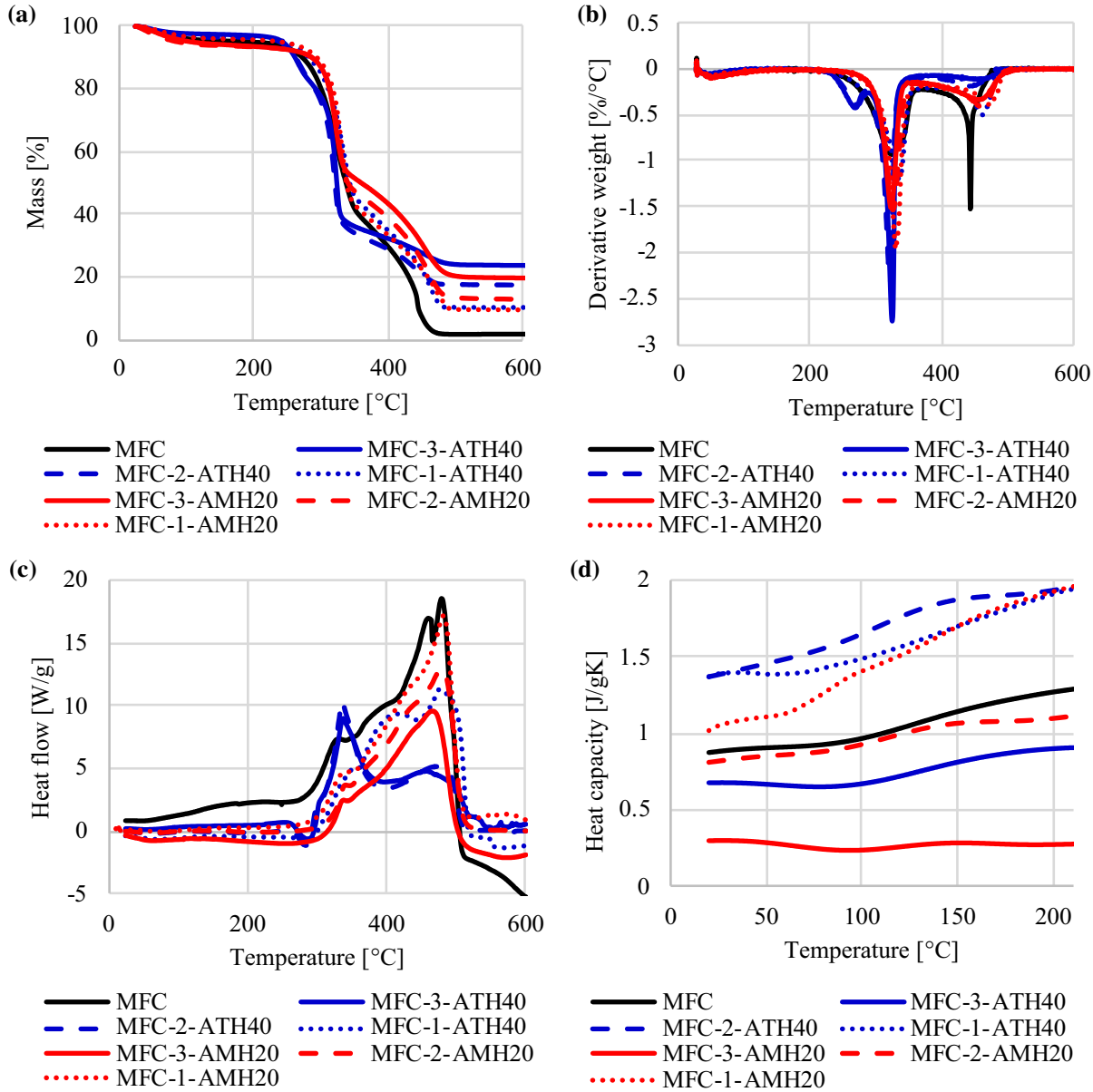

Fig. 8 **a** Thermo-gravimetric (TG), **b** Derivative weight (DTG) **c** Heat-flow (DSC) analysis and **d** Heat-capacity curves of different MFC-based films

polymorphic structure, their content and distribution through the film, as well as their transformation through the heating. The smaller and meta-stable AlO(OH) particles with large surface area and gradual decomposition thus resulted to optically transparent and thermally the most stable film, with higher heat transition / dissipating ability, and an increased tensile strength and Young's modulus. This showed their potential applications in flexible and transparent opto-electronics to cool the device, or in thermal sensitive packaging materials to protect the products from external heating. In addition, a hydrophobic surface with low oxygen permeability shows that such a film is also useful in eco-benign food packaging.

Table 2 Relevant data about the thermal decomposition process of different MFC-based films and Specific heat capacity (Cp) values at certain temperatures

		MFC	ATH40			AMH20		
			3	2	1	3	2	1
Weight loss 25–200 °C [%]		4.94	2.96	3.58	3.71	6.57	6.36	4.21
Onset decomp. temp (2nd step) [°C]		281	260	262	279	305	305	307
Residual weight at 600 °C [%]		1.8	23.3	17.1	10.1	20.1	12.6	9.9
Enthalpy [J/g]		13,100	5576	5918	10,700	7598	8385	9588
Enthalpy change (in regard to MFC) [%]		–	−57	−55	−18	−42	−36	−26
Position of main exothermic peak [°C]		479	338	336	419	466	479	481
Cp values at certain temp. [J/gK]	20 °C	0.87	0.68	1.37	1.37	0.31	0.81	1.02
	100 °C	0.97	0.68	1.65	1.48	0.26	0.93	1.41
	150 °C	1.14	0.81	1.87	1.69	0.29	1.06	1.70
	200 °C	1.26	0.89	1.93	1.90	0.28	1.09	1.93

Funding This research was funded by the Slovenian Research Agency (Grant No. L2-9249 and Research Program P2-0118).

Declarations

Conflicts of interest The authors declare no conflict of interest.

References

Abdollahifar M, Hidaryan M, Jafari P (2018) The role anions on the synthesis of AlOOH nanoparticles using simple solvothermal method. Boletín De La Sociedad Española De Cerámica y Vidrio 57(2):66–72. https://doi.org/10.1016/j.bsecv.2017.06.002

Abitbol T, Rivkin A, Cao Y, Nevo Y, Abraham E, Ben-Shalom T, Lapidot S, Shoseyov O (2016) Nanocellulose, a tiny fiber with huge applications. Curr Opin Biotechnol 3:76–88. https://doi.org/10.1016/j.copbio.2016.01.002

Acharya D, Mohanta B, Deb S, Sen A (2018) Theoretical prediction of absorbance spectra considering the particle size distribution using Mie theory and their comparison with the experimental UV–Vis spectra of synthesized nanoparticles. Spectrosc Lett 51:1–5. https://doi.org/10.1080/00387010.2018.1442351

Andresen M, Johansson L-S, Tanem BS, Stenius P (2006) Properties and characterization of hydrophobized microfibrillated cellulose. Cellulose 13(6):665–677. https://doi.org/10.1007/s10570-006-9072-1

Ballal D, Chapman WG (2013) Hydrophobic and hydrophilic interactions in aqueous mixtures of alcohols at a hydrophobic surface. J Chem Phys 139(11):114706. https://doi.org/10.1063/1.4821604

Beeran YPT, Bobnar V, Gorgieva S, Grohens Y, Finšgar M, Thomas S, Kokol V (2016) Mechanically strong, flexible and thermally stable graphene oxide/nanocellulosic films with enhanced dielectric properties. RSC Adv 6(54):49138–49149. https://doi.org/10.1039/C6RA06744A

Belbekhouche S, Bras J, Siqueira G, Chappey C, Lebrun L, Khelifi B, Marais S, Dufresne A (2011) Water sorption behavior and gas barrier properties of cellulose whiskers and microfibrils films. Carbohyd Polym 83(4):1740–1748. https://doi.org/10.1016/j.carbpol.2010.10.036

Beyer G (2001) Flame retardant properties of EVA-nanocomposites and improvements by combination of nanofillers

with aluminium trihydrate. Fire Mater 25(5):193–197. https://doi.org/10.1002/fam.776

Bunderšek A (2015) Influence of integration of Al(OH)3 nanoparticles on properties of cured acrylic composites. Dissertation, University of Maribor UDK: 66.095.26–97–022–17(043.3)

Bunderšek A, Japelj B, Mušič B, Rajnar N, Gyergyek S, Kostanjšek R, Krajnc P (2016) Influence of Al(OH)3 nanoparticles on the mechanical and fire resistance properties of poly(methyl methacrylate) nanocomposites. Polym Compos 37(6):1659–1666. https://doi.org/10.1002/pc.23338

Castro DO, Karim Z, Medina L, Häggström JO, Carosio F, Svedberg A, Wågberg L, Söderberg D, Berglund LA (2018) The use of a pilot-scale continuous paper process for fire retardant cellulose-kaolinite nanocomposites. Compos Sci Technol 162:215–224. https://doi.org/10.1016/j.compscitech.2018.04.032

Chen Q, Zeng W (1996) Calorimetric determination of the standard enthalpies of formation of gibbsite, Al(OH)3(cr), and boehmite, AlOOH(cr). Geochim Cosmochim Acta 60(1):1–5. https://doi.org/10.1016/0016-7037(95)00378-9

Cox JD, Wagman DD, Medvedev VA (1990) CODATA - Key Values for Thermodynamics. Hemisphere Publishing Corporation, New York, CODATA, Series on Thermodynamic Properties

Da Silva MA, Calabrese V, Schmitt J, Celebi D, Scott JL, Edler KJ (2018) Alcohol induced gelation of TEMPO-oxidized cellulose nanofibril dispersions. Soft Matter 14(45):9243–9249. https://doi.org/10.1039/C8SM01815D

De Salvi DTB, Barud HS, Caiut JMA, Messaddeq Y, Ribeiro SJL (2012) Self-supported bacterial cellulose/boehmite organic–inorganic hybrid films. J Sol-Gel Sci Technol 63:211–218. https://doi.org/10.1007/s10971-012-2678-x

Du X, Zhang Z, Liu W, Deng Y (2017) Nanocellulose-based conductive materials and their emerging applications in energy devices-A review. Nano Energy 35:299–320. https://doi.org/10.1016/j.nanoen.2017.04.001

Dufresne A (2013) Nanocellulose: a new ageless bionanomaterial. Mater Today 16(6):220–227. https://doi.org/10.1016/j.mattod.2013.06.004

Farooq M, Sipponen MH, Seppälä A, Österberg M (2018) Ecofriendly flame-retardant cellulose nanofibril aerogels by incorporating sodium bicarbonate. ACS Appl Mater Interfaces 10(32):27407–27415. https://doi.org/10.1021/acsami.8b04376

Favaro L, Boumaza A, Roy P, Lédion J, Sattonnay G, Brubach JB, Huntz A, TÉTot R, (2010) Experimental and ab initio infrared study of χ-, κ- and α-aluminas formed from gibbsite. J Solid State Chem 183:901–908. https://doi.org/10.1016/j.jssc.2010.02.010

Ghanadpour M, Wicklein B, Carosio F, Wågberg L (2018) All-natural and highly flame-resistant freeze-cast foams based on phosphorylated cellulose nanofibrils. Nanoscale 10(8):4085–4095. https://doi.org/10.1039/C7NR09243A

Gopakumar DA, Pai AR, Pottathara YB, Pasquini D, de Morais LC, Luke M, Kalarikkal N, Grohens Y, Thomas S (2018) Cellulose nanofiber-based polyaniline flexible papers as sustainable microwave absorbers in the X-Band. ACS Appl Mater Interfaces 10(23):20032–20043. https://doi.org/10.1021/acsami.8b04549

Gorgieva S, Jančič U, Hribernik S, Fakin D, Stana Kleinschek K, Medved S, Fakin T, Božič M (2020) Processing and functional assessment of anisotropic cellulose nanofibril/Alolt/sodium silicate: based aerogels as flame retardant thermal insulators. Cellulose 27(3):1661–1683. https://doi.org/10.1007/s10570-019-02901-3

Goudarzi M, Ghanbari D, Salavati-Niasari M, Ahmadi A (2016) Synthesis and characterization of Al(OH)3, Al2O3 nanoparticles and polymeric nanocomposites. J Cluster Sci 27(1):25–38. https://doi.org/10.1007/s10876-015-0895-5

Guo W, Wang X, Zhang P, Liu J, Song L, Hu Y (2018) Nanofibrillated cellulose-hydroxyapatite based composite foams with excellent fire resistance. Carbohyd Polym 195:71–78. https://doi.org/10.1016/j.carbpol.2018.04.063

Hasan MA, Zaki MI, Pasupulety L (2003) Oxide-catalyzed conversion of acetic acid into acetone: an FTIR spectroscopic investigation. Appl Catal A 243(1):81–92. https://doi.org/10.1016/S0926-860X(02)00539-2

He C, Huang J, Li S, Meng K, Zhang L, Chen Z, Lai Y (2018) Mechanically resistant and sustainable cellulose-based composite aerogels with excellent flame retardant, sound-absorption, and superantiwetting ability for advanced engineering materials. ACS Sustainable Chemistry & Engineering 6(1):927–936. https://doi.org/10.1021/acssuschemeng.7b03281

Herreros B, Klinowski J (1995) Influence of the source of silicon and aluminium in the hydrothermal synthesis of sodalite. J Chem Soc, Faraday Trans 91(7):1147–1154. https://doi.org/10.1039/FT9959101147

Horrocks AR (2011) Flame retardant challenges for textiles and fibres: New chemistry versus innovatory solutions. Polym Degrad Stab 96(3):377–392. https://doi.org/10.1016/j.polymdegradstab.2010.03.036

Hubbe M A, Ferrer A, Tyagi P, Yin Y, Salas C, Pal L, Rojas O (2017) Nanocellulose in thin films, coatings, and plies for packaging applications: A review. BioResources 12(1):2143–2233. http://urn.fi/URN:NBN:fi:aalto-201710157155

Hull TR, Witkowski A, Hollingbery L (2011) Fire retardant action of mineral fillers. Polym Degrad Stab 96(8):1462–1469. https://doi.org/10.1016/j.polymdegradstab.2011.05.006

Jiang L, Li K, Yang H, Liu X, Xu W, Deng B (2019) Significantly improved flame-retardancy of cellulose acetate nanofiber by Mg-based nano flaky petal. Cellulose 26:5211–5226. https://doi.org/10.1007/s10570-019-02451-8

Jin S, Li K, Li J (2018) Nature-inspired green procedure for improving performance of protein-based nanocomposites via introduction of nanofibrillated cellulose-stablized graphene/carbon nanotubes hybrid. Polymers 10(3):270. https://doi.org/10.3390/polym10030270

Karger-Kocsis J, Lendvai L (2018) Polymer/boehmite nanocomposites: A review. J Appl Polym Sci 135(24):45573. https://doi.org/10.1002/app.45573

Kaushik M, Moores A (2016) Review: nanocelluloses as versatile supports for metal nanoparticles and their applications in catalysis. Green Chem 18(3):622–637. https://doi.org/10.1039/C5GC02500A

Khalil KMS (2008) Formation of mesoporous alumina via hydrolysis of modified aluminum isopropoxide in presence

of CTAB cationic surfactant. Appl Surf Sci 255(5):2874–2878. https://doi.org/10.1016/j.apsusc.2008.08.091

Kim J-H, Lee D, Lee Y-H, Chen W, Lee S-Y (2019) Nanocellulose for energy storage systems: beyond the limits of synthetic materials. Adv Mater 31(20):1804826. https://doi.org/10.1002/adma.201804826

Köklükaya O, Carosio F, Wågberg L (2017) Superior flame-resistant cellulose nanofibril aerogels modified with hybrid layer-by-layer coatings. ACS Appl Mater Interfaces 9(34):29082–29092. https://doi.org/10.1021/acsami.7b08018

Kumar V, Bollström R, Yang A, Chen Q, Chen G, Salminen P, Bousfield D, Toivakka M (2014) Comparison of nano- and microfibrillated cellulose films. Cellulose 21(3):3443–3456. https://doi.org/10.1007/s10570-014-0357-5

Lamouri S, Hamidouche M, Bouaouadja N, Belhouchet H, Garnier V, Fantozzi G, Trelkat JF (2017) Control of the γ-alumina to α-alumina phase transformation for an optimized alumina densification. Boletín De La Sociedad Española De Cerámica y Vidrio 56(2):47–54. https://doi.org/10.1016/j.bsecv.2016.10.001

Laoutid F, Bonnaud L, Alexandre M, Lopez-Cuesta JM, Dubois P (2009) New prospects in flame retardant polymer materials: From fundamentals to nanocomposites. Mater Sci Eng R Rep 63(3):100–125. https://doi.org/10.1016/j.mser.2008.09.002

Li Y, Wang B, Sui X, Xu H, Zhang L, Zhong Y, Mao Z (2017) Facile synthesis of microfibrillated cellulose/organosilicon/polydopamine composite sponges with flame retardant properties. Cellulose 24(9):3815–3823. https://doi.org/10.1007/s10570-017-1373-z

Lichtenstein K, Lavoine N (2017) Toward a deeper understanding of the thermal degradation mechanism of nanocellulose. Polym Degrad Stab 146:53–60. https://doi.org/10.1016/j.polymdegradstab.2017.09.018

Lin W, Hu X, You X, Sun Y, Wen Y, Yang W, Zhang X, Li Y, Chen H (2018) Hydrophobic modification of nanocellulose via a two-step silanation method. Polymers 10(9):1035. https://doi.org/10.3390/polym10091035

Lu J, Askeland P, Drzal LT (2008) Surface modification of microfibrillated cellulose for epoxy composite applications. Polymer 49(5):1285–1296. https://doi.org/10.1016/j.polymer.2008.01.028

Lyytikäinen J, Morits M, Österberg M, Heiskanen I, Backfolk K (2021) Skin and bubble formation in films made of methyl nanocellulose, hydrophobically modified ethyl(hydroxyethyl)cellulose and microfibrillated cellulose. Cellulose 28:787–797. https://doi.org/10.1007/s10570-020-03557-0

Machrafi H, Lebon G, Iorio CS (2016) Effect of volume-fraction dependent agglomeration of nanoparticles on the thermal conductivity of nanocomposites: applications to epoxy resins, filled by SiO2, AlN and MgO nanoparticles. Compos Sci Technol 130:78–87. https://doi.org/10.1016/j.compscitech.2016.05.003

Mastalska-Popławska J, Pernechele M, Troczynski T, Izak P (2017) Thermal properties of silica-coated cellulose fibers for increased fire-resistance. J Sol-Gel Sci Technol 83(3):683–691. https://doi.org/10.1007/s10971-017-4445-5

Miyashiro D, Hamano R, Umemura U (2020) A review of applications using mixed materials of cellulose, nanocellulose and carbon nanotubes. Nanomaterials 10(2):186. https://doi.org/10.3390/nano10020186

Norouzi M, Zare Y, Kiany P (2015) Nanoparticles as effective flame retardants for natural and synthetic textile polymers: application, mechanism, and optimization. Polym Rev 55(3):531–560. https://doi.org/10.1080/15583724.2014.980427

Oun AA, Shankar S, Rhim J-W (2020) Multifunctional nanocellulose/metal and metal oxide nanoparticle hybrid nanomaterials. Crit Rev Food Sci Nutr 60(3):435–460. https://doi.org/10.1080/10408398.2018.1536966

Radionova G, Hoff B, Lenes M et al (2013) Gas-phase esterification of microfibrillated cellulose (MFC) films. Cellulose 20:1167–1174. https://doi.org/10.1007/s10570-013-9887-5

Rahmanpour O, Shariati A, Khosravi-Nikou MR (2012) New method for synthesis nano size γ-Al2O3 catalyst for dehydration of methanol to dimethyl ether. Int J Chem Eng Appl 3(2):125–128. https://doi.org/10.7763/IJCEA.2012.V3.172

Reddy T, Thyagarajan K, Almanza O, Sanapa-Reddy L, Endo T (2014) X-ray diffraction, electron paramagnetic resonance and optical absorption study of bauxite. J Min Mat Characterization Eng 2:114–120. https://doi.org/10.4236/jmmce.2014.22015

Rodinova G, Hoff B, Lenes M, Eriksen O, Gregersen O (2013) Gas-phase esterification of microfibrillated cellulose (MFC) films. Cellulose 20(3):1167–1174. https://doi.org/10.1007/s10570-013-9887-5

Sathish S, Chandar Shrekar B, Chandru Kannan S, Sengodan R, Dinesh K, Ranjithkumar R (2015) Wide band gap transparent polymer-inorganic composite thin films by dip-coating method: preparation and characterizations. Int J Polym Anal Charact 20(1):29–41. https://doi.org/10.1080/1023666X.2015.975414

Sato K, Tominaga Y, Imai Y (2020) Nanocellulose and related materials applicable in thermal management of eletronic devices: A review. Nanomaterials 10(3):448459. https://doi.org/10.3390/nano10030448

Schawe JEK, Hütter T, Heitz C, Alig I, Lellinger D (2006) Stochastic temperature modulation: a new technique in temperature-modulated DSC. Thermochim Acta 446(1–2):147–155. https://doi.org/10.1016/j.tca.2006.01.031

Sifontes A, Gutiérrez B, Mónaco A, Yanez A, Diaz Y, Mendez F, Llovera L, Cañizales E, Brito J (2014) Preparation of funcionalized porous nano-γ-Al2O3 powders employing colophony extract. Biotechnol Rep 4:21–29. https://doi.org/10.1016/j.btre.2014.07.001

Sing KS (1985) Reporting physisorption data for gas/solid systems with special reference to the determination of surface area and porosity (Recommendations 1984). Pure Appl Chem 57(4):603–619. https://doi.org/10.1351/pac198557040603

Singh S, Gaikwad KK, Lee M, Lee ZS (2018) Temperature-regulating materials for advanced food packaging applications: a review. J Food Measurement Characterization 12:588–601. https://doi.org/10.1007/s11694-017-9672-5

Syverud K, Stenius P (2008) Strength and barrier properties of MFC films. Cellulose 16:75–85. https://doi.org/10.1007/s10570-008-9244-2

Wang L, Cui L, Sánchez-Soto M, Shou W, Xia Z, Liu Y (2018) Highly flame retardant melamine-formaldehyde cross-linked cellulose nanofibrils/sodium montmorillonite aerogels with improved mechanical properties. Macromol Mater Eng 303(10):1800379. https://doi.org/10.1002/mame.201800379

Wen J (2007) Heat Capacities of Polymers. In: Mark JE (ed) Physical properties of polymers Handbook. SpringerMaterials, New York, pp 145–154. https://materials.springer.com/lb/docs/sm_nlb_978-0-387-69002-5_9

Wicklein B, Kocjan A, Salazar-Alvarez G, Carosio F, Camino G, Antonietti M, Bergström L (2014) Thermally insulating and fire-retardant lightweight anisotropic foams based on nanocellulose and graphene oxide. Nat Nanotechnol 10:277–283. https://doi.org/10.1038/nnano.2014.248

Wu C-N, Saito T, Yang Q, Fukuzumi H, Isogai A (2014) Increase in the water contact angle of composite film surfaces caused by the assembly of hydrophilic nanocellulose fibrils and nanoclay platelets. ACS Appl Mater Interfaces 6(15):12707–12712. https://doi.org/10.1021/am502701e

Yang F, Zhang Y, Feng Y (2017) Adding aluminum hydroxide to plant fibers using in situ precipitation to improve heat resistance. BioResources 12(1):1826–1834. https://doi.org/10.15376/biores.12.1.1826-1834

Yang S, Xie Q, Liu X, Wu M, Wang S, Song X (2018) Acetylation improves thermal stability and transmittance in FOLED substrates based on nanocellulose films. RSC Adv 8(7):3619–3625. https://doi.org/10.1039/C7RA11134G

Yuan B, Zhang J, Yu J, Song R, Mi Q, He J, Zhang J (2016) Transparent and flame retardant cellulose/aluminum hydroxide nanocomposite aerogels. SCIENCE CHINA Chem 59(10):1335–1341. https://doi.org/10.1007/s11426-016-0188-0

Zeng Z, Wu T, Han D, Ren Q, Siqueira G, Nyström G (2020) Ultralight, flexible, and biomimetic nanocellulose/silver nanowire aerogels for electromagnetic interference shielding. ACS Nano 14(3):2927–2938. https://doi.org/10.1021/acsnano.9b07452

Zhang T, Zhao X, Poon R, Clifford A, Mathews R, Zhitomirsky I (2017) Synthesis and liquid-liquid extraction of non-agglomerated Al(OH)3 particles for deposition of cellulose matrix composite films. J Colloid Interface Sci 508:49–55. https://doi.org/10.1016/j.jcis.2017.08.026